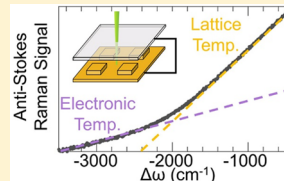


# Photothermalization and Hot Electron Dynamics in the Steady State

Nicki Hogan,<sup>†</sup> Shengxiang Wu,<sup>†</sup> and Matthew Sheldon\*,<sup>†,‡</sup><sup>†</sup>Department of Chemistry, Texas A&M University, College Station, Texas 77843-3255, United States<sup>‡</sup>Department of Material Science and Engineering, Texas A&M University, College Station, Texas 77843-3255, United States

**ABSTRACT:** Significant recent interest in plasmonic nanomaterials is based on the ability to use the strong resonant absorption to produce large transient populations of photoexcited non-equilibrium “hot” carriers that can then be employed in novel classes of photochemical reactions and more general optoelectronic detection schemes and power cycles. In this Feature Article, we outline nanoscale design features that allow for systematic control over photothermalization in plasmonic materials, connecting the microscopic mechanism of absorption, photoexcitation, relaxation, and thermal emission with the electronic temperature and lattice temperature of a metal during steady state illumination. Further, we show how anti-Stokes Raman spectroscopy can provide a quantitative measure of the energy distribution of the hot electrons and the surrounding lattice temperature, as well as indicate the electron–phonon coupling constant of hot electrons, all under optical conditions relevant to emerging hot electron devices, i.e., relatively low fluence, continuous wave (CW) excitation. A major insight from our experiments is the presence of a sustained subpopulation of hot electrons at an elevated temperature in comparison with the majority of the conduction electrons in the metal. In conjunction, we show what features of nanoscopic geometries give rise to the largest population and longest-lived hot electrons, as required for the goals of optimizing electron dynamics in developing applications of plasmonic hot electrons.



## INTRODUCTION

Plasmonic resonances, the coherent mechanical oscillation of free charge carriers at optical frequencies inside nanoscale conductors, have now been studied for decades by chemists, starting with some of the earliest analyses of surface enhanced Raman spectroscopy (SERS) on nanostructured metals.<sup>1</sup> Because these resonances support extreme optical confinement into subwavelength volumes at hot spots near the nanostructure’s surface, several classes of subwavelength optical imaging, detection, and single molecule sensing have been developed.<sup>2–4</sup> More broadly, researchers across disciplines have refined understanding of the design space of plasmonic materials for more systematic control of light–matter interactions, culminating today in macroscopic “metamaterials” composed of plasmonic subunits that support exotic optical responses, such as unity absorption or transmission, negative index of refraction, pronounced circular dichroism, or enhancement of a variety of nonlinear phenomena.<sup>5–7</sup>

As we describe in more detail below, such control over the optical response also enables unique opportunities for defining the wavelength dependent and angle dependent absorption cross section of metals across a broad spectral range, from UV to mid-IR, and thereby resonant photothermal energy concentration from optically induced heating. Because metals exhibit a very low efficiency for photoluminescence (<10<sup>-6</sup> %),<sup>8</sup> nearly all optical energy absorbed is thermalized as vibrational energy in the metal. Indeed, one of the most intriguing developments in plasmonics is the use of the materials to provide extreme localized heating for use in cancer therapy.<sup>9</sup> In addition, researchers have used the tailorability of the optical response for several classes of nanoscale heat engines that leverage optically induced heating in power cycles, such as solar-powered water heating, distillation, or thermoelectric power generation.<sup>10–12</sup>

However, before optical absorption dissipates as vibrational heating in the surrounding environment, there are several microscopic steps that characterize the relaxation of the short-lived subpopulation of photoexcited carriers. As established by a wealth of recent *ab initio* calculations and confirmed in ultrafast transient absorption (TA) studies, optical absorption in plasmonic nanostructures occurs primarily via Landau damping and bulk losses such as interband absorption.<sup>13</sup> Which mechanism dominates is dependent on the size of the nanostructure, with bulk losses dominating in nanostructures with lateral dimensions larger than ~10 nm.<sup>14,15</sup> Optical excitation instantaneously provides an excited state distribution of electrons and holes that depends on the frequency of excitation, optical power, and the characteristic transition dipoles of the absorber. Within femtoseconds, this nonthermal subpopulation of excited carriers undergoes electron–electron scattering to achieve a distribution of “hot” electrons with a characteristic temperature that, during intense ultrashort pulsed excitation, can be several 1000 K greater than the ambient temperature of the metal lattice.<sup>16</sup> Within picoseconds, the carriers further relax via phonon coupling to induce vibrational excitations of the metal lattice. Depending on the thermal impedance with the environment and the absorbed optical power, the lattice temperature of the plasmonic absorber can also be significantly increased. However, given the large difference in the heat capacity of the electron gas compared with the metal lattice, the vibrational temperature increase is usually significantly lower than the electronic temperature increase, with reports of lattice temperature increases of ~1 K to

Received: September 19, 2019

Revised: November 12, 2019

Published: December 10, 2019

hundreds of K, depending on optical fluence.<sup>17,18</sup> Notably, solar-induced vaporization of water around colloidal SiO<sub>2</sub>/Au nanoparticles has been reported.<sup>19</sup> In general, increases in lattice temperature also allow for the metal to reach higher electronic temperatures, as we describe below.<sup>20</sup>

The physical picture of the dynamics of the hot carriers observed in TA studies is summarized in the well-established two-temperature model (TTM), where the time dependence of energy transfer between the excited electrons and the metal lattice is defined by the electron–phonon coupling constant,  $G$ , the thermal transport of energy away from the absorbing region, depending on the electronic thermal conductivity,  $k_e$ , and the electronic and lattice heat capacities,  $C_e$  and  $C_l$ , respectively.<sup>16</sup>

$$C_e \frac{\partial T_e}{\partial t} = \nabla [k_e \nabla T_e] - G(T_e - T_l) \quad (1)$$

$$C_l \frac{\partial T_l}{\partial t} = G(T_e - T_l) \quad (2)$$

These equations show that the rate at which the thermal energy in the electron gas is converted to vibrational energy is proportional to the temperature difference between the lattice,  $T_l$ , and the electrons,  $T_e$  (eq 2). Note that nanoscale subwavelength metal absorbers may have no significant thermal gradients in electronic temperature if the absorber is on the scale of the optical penetration depth into the metal ( $\sim 10$ – $20$  nm), so that the term dependent on  $k_e$  often can be neglected. Often, this TTM is extended into the so-called “expanded TTM” which accounts for not only electrons thermalized to  $T_e$  and  $T_l$  but also the short-lived nonthermalized portion of the electrons before electron–electron scattering has occurred.<sup>20–22</sup>

Some of the most fast-developing recent research in plasmonics explores the opportunities for using the photoexcited carriers for photochemistry or optoelectronic devices in the short period of time before they thermalize with the lattice. Reports of solar-powered water splitting and CO<sub>2</sub> reduction as well as photoactivated plasmonic antenna-reactor systems illustrate the vast interest in these non-equilibrium electrons.<sup>23–25</sup> Major challenges are twofold. First, given the short fs lifetime before electron–electron scattering establishes a thermal distribution,  $T_e$ , the mean-free path for a photoexcited, nonthermal electron or hole is  $\sim 100$  nm or less. Thus, carriers with the highest kinetic energy are very short-lived, compared with the “hot” electrons in the thermal distribution  $T_e$ . Even still, the lifetime of hot carriers is also short, thermalizing with the lattice within  $\sim$ ps. Additionally, there is a limited escape cone of electron or hole trajectories with suitable momentum to exit the metal. Notably, nanoscopic confinement increases the probability that a hot electron will both reach a surface and have appropriate momentum for collection in an external device or chemical reaction.

To date, TA studies of the relaxation of the electron gas after optical excitation using ultrafast pump–probe geometries have been a primary tool for understanding plasmonic photodynamics. In combination with the expanded TTM, it is possible to gain a significant amount of information about the time scales of thermalization, both on the femtosecond scale of electron–electron scattering and on the longer picosecond time scale that encapsulates electron–phonon interactions.<sup>20,22,26</sup> These studies have provided a quantitative measure of the lifetime of electrons in the non-equilibrium distribution and the electron–phonon coupling constant,  $G$  in eqs 1 and 2, which connects the lifetime to microscopic loss pathways in the

metal.<sup>27</sup> This research has also provided several other insights, including evidence for direct excitation into charge-transfer states at the interface of the metal with a semiconductor or molecule<sup>28</sup> and the observation of coherent excitation of vibrational modes in plasmonic nanoparticles after pulsed excitation.<sup>13</sup>

In addition to what can be understood by the dynamics observed in pump–probe studies, there is also much interest in the hot electron response during CW optical excitation, such as what can be achieved with devices or photochemical systems under solar illumination. Under these steady state conditions, there will always be a subpopulation of electrical carriers present with greater kinetic energy than electrons that have relaxed and equilibrated with the lattice. Moreover, the dynamics of hot carriers in this prolonged time regime, and at significantly lower optical intensity than in ultrafast pump–probe studies, is much less understood. In this Feature Article, we outline how the emission and absorption properties of plasmonic materials can be optimized in order to obtain the highest possible temperatures during photothermalization. Building from this framework, we then provide new insight into the steady state behavior of hot electrons under CW illumination. We have recently refined an anti-Stokes Raman spectroscopy technique that probes the energetic distribution of electrons in plasmonic nanostructures during CW excitation.<sup>29</sup> We show how the technique provides a quantitative measure of a sustained subpopulation of hot electrons at an elevated temperature distribution,  $T_e$ , in addition to electrons that are in equilibrium with the lattice temperature,  $T_l$ . The physical picture is that, in the steady state, photoexcited electrons thermalize very quickly with other hot electrons via electron–electron scattering ( $\sim$ fs), well before relaxing to the bath electron distribution that is equilibrated with the lattice ( $\sim$ ps). Because these dynamics result from the distinct time scales that give rise to the TTM described above, this Raman technique additionally gives information about the electron–phonon coupling constant, for comparison with more-established TA methods, while at much lower CW optical excitation intensity. Just as the design rules for maximizing photothermal energy concentration for lattice heating have been well established in the plasmonics literature, this report provides new insights into how the non-equilibrium hot electron temperature can also be understood and controlled in the steady state, for emerging applications of plasmonic hot electrons.

## METHODS

**Fabrication.** To prepare plasmonic nanostructures, a 5 nm Cr sticking layer was thermally evaporated onto a Si wafer followed by a 150 nm gold film (Lesker PVD e-beam evaporator). Nanoscale patterns were deposited on these substrates using electron beam lithography. A resist layer of PMMA/MMA 9% in ethyl lactate (MicroChem) followed by a layer of 2% 950k PMMA in anisole (MicroChem) were spin coated. Exposure of the resist to an electron beam for lithography was performed using a Tescan FE-SEM instrument. A 100 nm gold layer was evaporated on top before the resist was removed in acetone.

**Spectroscopy.** Reflection spectra were taken using a confocal microscope (Witec RA300) with a 100 $\times$  objective (0.9 NA) and a white light illumination source. Reflection measurements were normalized to the source spectra to calculate absorptivity. Anti-Stokes Raman spectra were collected on the same instrument with a vacuum heating stage attached to

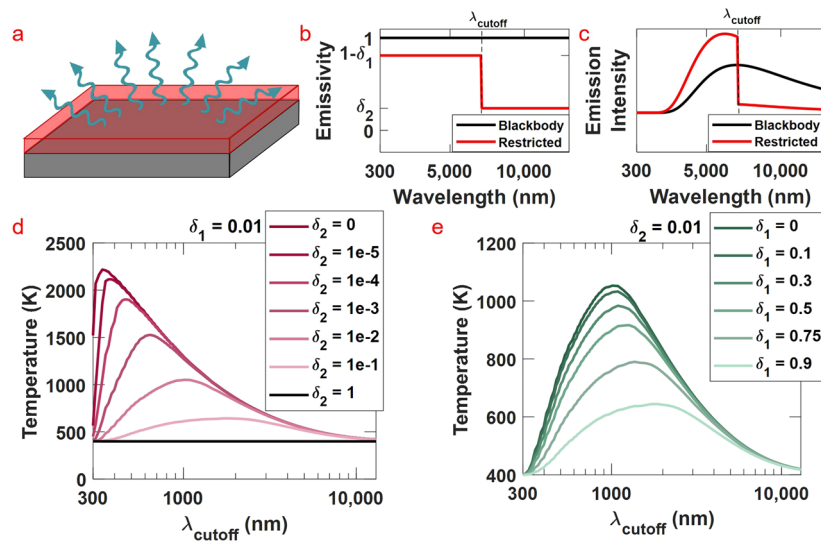


**Figure 1.** (a) Schematic of a selective absorber optimized for solar heating along with (b) the emissivity function (red trace) compared to a blackbody (black trace) and (c) the relative spectral emission intensity compared with a blackbody when both absorbers are in direct sunlight. The blackbody reaches  $T = 410$  K, and the depicted selective absorber with  $\delta_1 = \delta_2 = 0.1$  and  $\lambda_{\text{cutoff}} = 7100$  nm reaches  $T = 643$  K. Parts d and e show the possible temperatures that can be obtained by modifying emission in either the high or low wavelength region of the spectrum as a function of  $\lambda_{\text{cutoff}}$ .

a vacuum pump (Linkam TS1500VE). Vacuum measurements were performed at a pressure of 0.010 mbar. Samples were illuminated with a 532 nm CW Nd:Yag laser which was focused on the sample with a 20 $\times$  objective (0.4 NA).

**Electrical Measurements.** The nanostructured gold patterns and an ITO coated glass slide were secured together in a parallel plate geometry with a 200  $\mu\text{m}$  bilayer spacer composed of Kapton tape (on the ITO side) and copper tape (attached to the gold film surrounding the nanostructures). The sample was placed in the same microscope stage (Linkam TS1500VE) and brought to a pressure of 0.010 mbar. A 532 nm CW diode laser was focused on the surface with a 50 $\times$  objective (0.55 NA), and electrodes were connected to a source-measure unit (Keithley 2450) to vary the bias while measuring current. The laser light was chopped at 47 Hz, and current was measured using a lock-in amplifier (Stanford Research Systems, SR830). Bias voltage was modulated between -0.2 V (accelerating bias) and 1 V (retarding bias) for each optical power.

## ■ PHOTOTHERMALIZATION AND LATTICE TEMPERATURE IN THE STEADY STATE

Researchers in plasmonics, and nano-optics more broadly, have developed design rules for maximizing the lattice temperature of an optical absorber due to photothermalization by modifying the spectrally dependent and angle dependent absorptivity,  $\alpha(\lambda, \theta, \phi)$ . This parameter is highly tunable due to the dependence of the plasmon resonance on the size, shape, and surrounding dielectric environment of a subwavelength metal. Thermal emissivity,  $\epsilon(\lambda, \theta, \phi)$ , is the parameter that describes how a material emits thermal radiation into the surrounding environment. For a material at a given temperature,  $\epsilon$  corresponds to the scaling factor for emission according to a Planck distribution. Ideal blackbodies absorb light from all angles and at all wavelengths with  $\alpha(\lambda, \theta, \phi) = 1$ , and similarly, blackbodies emit radiation into all angles uniformly with a spectral profile based on temperature as described by the Planck distribution. Real materials, or gray bodies, take values of  $\alpha(\lambda, \theta, \phi) < 1$  and  $\epsilon(\lambda, \theta, \phi) < 1$ . According to Kirchhoff's law of radiation,  $\alpha(\lambda, \theta, \phi)$  and  $\epsilon(\lambda, \theta, \phi)$  are equivalent. Due to the original derivation of

Kirchoff's law as a consequence of thermal equilibrium, there has been some debate about its validity for plasmonic systems, especially when there may be a significant population of non-equilibrium hot electrons. However, recent reports have provided arguments to justify the local equivalence of absorption rate and emission rate in plasmonic systems.<sup>30</sup> Thus, defining the absorption properties of a material also controls how the material emits thermal radiation, and therefore how it radiatively equilibrates the energy it absorbs with the surrounding environment.

Intuitively, to maximize the temperature of an absorber, the goal is to maximize the cross section for absorption at incident optical frequencies but minimize the efficiency of thermal emission, while also minimizing thermal energy transfer through conduction or convection. This strategy has been well established, for example, for use in thermophotovoltaic schemes, or in other applications of solar-thermal heating.<sup>31</sup> For these applications, so-called "selective absorbers" are designed that maximize the absorption of the incident solar spectrum while maintaining very low radiative emission in the infrared (IR). Because of the low efficiency for IR emission, in the steady state, selective absorbers must reach much higher internal temperatures in order to radiate the same power that is absorbed from the sun, as depicted schematically in Figure 1.

We can better understand the desired properties for photothermal heating by examining the basic relations that account for this power balance between optical absorption and thermal emission. Here we consider an absorber that is in direct sunlight. As shown in eq 3, the radiative power absorbed,  $P_{\text{abs}}$ , must equal the power emitted,  $P_{\text{emit}}$ , though not necessarily in the same spectral range.

$$P_{\text{abs}} = P_{\text{emit}} \quad (3)$$

The power absorbed is related to the fraction of energy from sunlight that is absorbed,  $P_{\text{sun}}$ , and depends on the absorptivity of the material,  $\alpha(\lambda, \theta, \phi)$ , as well as the spectral and angular profile of sunlight,  $I_{\text{solar}}(\lambda, \theta, \phi)$ . In addition to sunlight, the absorber will take in radiative energy from the ambient

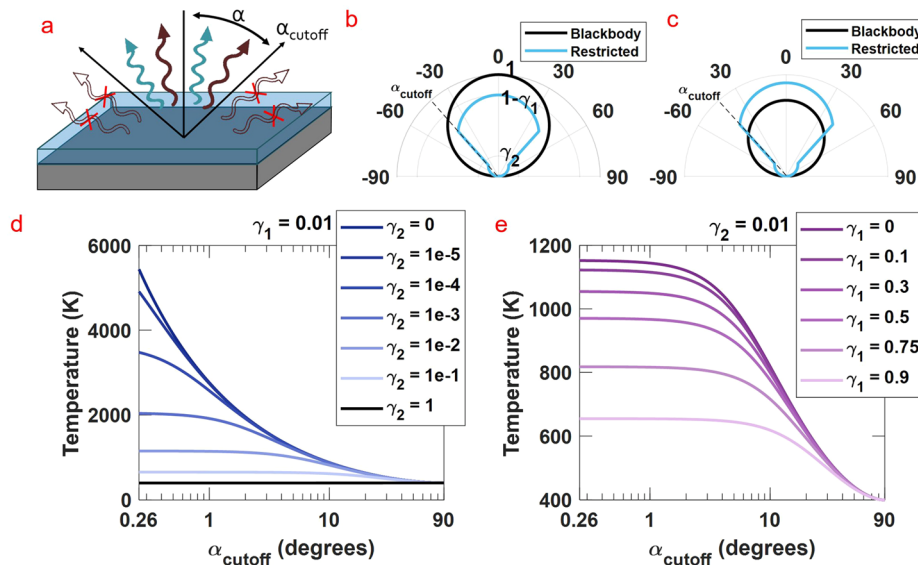


**Figure 2.** (a) Schematic of an angle selective surface along with (b) the emissivity function (blue trace) compared to a blackbody (black trace) and (c) the relative emission intensity compared to a blackbody when both absorbers are under full sun at normal incidence. The blackbody reaches  $T = 410$  K, and the angle selective surface depicted here, with  $\gamma_1 = \gamma_2 = 0.2$  and  $\alpha_{\text{cutoff}} = 40^\circ$ , reaches  $T = 653$  K. Parts d and e show the possible temperatures that can be obtained by modifying emission in either the high or low angle range as a function of  $\alpha_{\text{cutoff}}$ .

environment,  $P_{\text{amb}}$ , described by a Plank distribution at temperature  $T_{\text{amb}}$ .

$$P_{\text{abs}} = P_{\text{sun}} + P_{\text{amb}} \quad (4)$$

$$P_{\text{sun}} = \int_{0^\circ}^{360^\circ} \int_{0^\circ}^{0.26^\circ} \int_0^\infty \alpha(\lambda, \theta, \phi) I_{\text{solar}}(\lambda, \theta, \phi) \cos \theta \sin \theta \, d\lambda \, d\theta \, d\phi \quad (5)$$

$$P_{\text{amb}} = \int_{0^\circ}^{360^\circ} \int_{0^\circ}^{90^\circ} \int_0^\infty \alpha(\lambda, \theta, \phi) \frac{2hc^2}{\lambda^5} \frac{1}{e^{(hc/\lambda kT_{\text{amb}})} - 1} \cos \theta \sin \theta \, d\lambda \, d\theta \, d\phi \quad (6)$$

In the following calculations, integration over the zenith angle,  $\theta$ , is limited to a hemispherical area to account for a surface that is only absorbing and emitting from the top face, a situation that is realized when a mirror is on the underside of the structure. We integrate the power absorbed over the solid angle subtended by the sun,  $0.26^\circ$ .<sup>32</sup> The absorber will emit energy according to its emissivity function and internal temperature,  $T$ , as indicated by  $P_{\text{radiative}}$ . In addition to radiative emission, the absorber may lose power through conduction, convection, or other nonradiative pathways,  $P_{\text{nonradiative}}$ .

$$P_{\text{emit}} = P_{\text{radiative}} + P_{\text{nonradiative}} \quad (7)$$

$$P_{\text{amb}} = \int_{0^\circ}^{360^\circ} \int_{0^\circ}^{90^\circ} \int_0^\infty \epsilon(\lambda, \theta, \phi) \frac{2hc^2}{\lambda^5} \frac{1}{e^{(hc/\lambda kT)} - 1} \cos \theta \sin \theta \, d\lambda \, d\theta \, d\phi \quad (8)$$

If the incident spectrum is known and power losses due to nonradiative pathways are understood or eliminated, the temperature,  $T$ , that an absorber reaches in the steady state is a unique function of the spectral absorptivity,  $\alpha(\lambda, \theta, \phi)$ , given the equality  $\epsilon(\lambda, \theta, \phi) = \alpha(\lambda, \theta, \phi)$ . Based on this framework, an ideal blackbody with  $\epsilon(\lambda, \theta, \phi) = \alpha(\lambda, \theta, \phi) = 1$  under the Air Mass 1.5 solar spectrum in an ambient environment at room temperature ( $T_{\text{amb}} = 298$  K) is expected to reach a temperature of 410 K, if nonradiative power losses are negligible. In general,

the highest possible temperatures are obtained when the power balance is dominated by radiative effects.

Before discussing the specific geometries we have fabricated that maximize photothermal heating, it is helpful to analyze how systematic control over  $\epsilon$  can lead to very dramatic increases in temperature, according to the behavior modeled in eqs 3–8 above and assuming negligible  $P_{\text{nonradiative}}$ . As shown schematically in Figure 1a, we consider a generalized absorber for which the surface has been modified through nanostructuring to provide a step function in the spectral absorptivity, or emissivity equivalently. The surface provides strong absorption for wavelengths below some cutoff,  $\lambda_{\text{cutoff}}$ , and weak absorption at longer wavelengths (Figure 1b). Our analysis also considers how deviations from an ideal step function impact temperature, with  $\delta_1$  accounting for deviations at short wavelengths and  $\delta_2$  accounting for deviations at long wavelengths. To date, plasmonic materials have been fabricated that demonstrate near unity absorptivity in the visible spectral region<sup>33,34</sup> and noble metal films intrinsically exhibit  $\epsilon \sim 0.01$  in the IR spectral region. For comparison, the spectral emissivity of an ideal blackbody is also depicted (Figure 1b, black line).

As can be clearly seen in Figure 1c, the presence of the step function in the emissivity profoundly impacts the spectral distribution of the emitted radiation, in comparison with the emission from a blackbody. Both the red and black trace in Figure 1c show thermal emission due to solar absorption. This change in the emission profile, with more photons emitted at higher energy, entails that the selective absorber is at a higher temperature due to the dependence on temperature in the Plank distribution and the requirement that both surfaces emit the same total power that they absorb. In this figure, the blackbody has reached a temperature of 410 K, while the selective absorber has reached a temperature of 643 K.

In Figure 1d and e, we consider how temperature is impacted by the spectral position of  $\lambda_{\text{cutoff}}$  as well as the dependence on the magnitude of  $\delta_1$  and  $\delta_2$ . First, as summarized in Figure 1d, it is clear that the highest possible temperatures are obtained when the long wavelength emissivity is kept as close as possible to zero.

The maximum temperature obtained is highly sensitive to very small changes as  $\delta_2$  approaches zero. This indicates that the temperature is more sensitive to small decreases in thermal emission, rather than increases in solar absorption. Decreasing emissivity at long wavelengths also blue shifts the  $\lambda_{\text{cutoff}}$  that provides the maximum temperature, until  $\lambda_{\text{cutoff}}$  is shifted so far to the blue that it impedes solar absorption. If however the long wavelength emissivity is fixed at a value comparable to the intrinsic emissivity of a noble metal film,  $\epsilon = 0.01$  (Figure 1e), then the dependence on deviations from perfect absorption at short wavelengths is less pronounced. Across the entire range of values for  $\delta_1$ , the spectral position of  $\lambda_{\text{cutoff}}$  that provides the highest temperature is maintained between 1000 and 2000 nm and the maximum temperature is between 600 and 1200 K. Nonetheless, this is still a significant increase in temperature compared with the temperature of 410 K that a blackbody obtains in full sun.

Another powerful way to affect the thermal energy balance of an optical absorber and increase temperature is to constrain the angular range of thermal emission, as depicted in Figure 2a. In analogy with the analysis of modifications to spectral emissivity discussed above, we consider a nanostructured surface that has been designed to strongly absorb and emit radiation only within a specific solid angle range around normal incidence. This solid angle range is defined by  $\alpha_{\text{cutoff}}$  with absorption or emission into larger angles prohibited. In the analysis that follows, we assume that the sun is at normal incidence, so that the radius of the solid angle subtended by the solar disk extends to  $0.26^\circ$  from the surface normal.<sup>35</sup> The emissivity function is depicted in profile in polar coordinates in Figure 2b, assuming radial symmetry around the normal axis in all calculations. The  $\cos(\theta)$  dependence that characterizes the Lambertian emission of radiation from a point on the surface of a blackbody is also depicted (black trace). Further, deviations from a perfect step function in the angle dependent emissivity are represented by  $\gamma_1$  at low angles around normal incidence and  $\gamma_2$  at high angles. Figure 2c shows how the emission intensity from a surface with  $\alpha_{\text{cutoff}} = 42^\circ$  is increased at small angles compared with a blackbody, due to the change in the angle dependent emissivity. As above, in accordance with eqs 3–8, this increase in emission intensity into some angles entails that this angle selective absorber is at a higher temperature (653 K) compared with a blackbody (410 K) when absorbing light from the sun.

We also analyze how temperature is impacted by the choice of  $\alpha_{\text{cutoff}}$  including the dependence on  $\gamma_1$  and  $\gamma_2$  (Figure 2d,e). As  $\gamma_1$  and  $\gamma_2$  both approach zero, the temperature that can be reached by the surface is increased, with higher temperatures obtained as  $\alpha_{\text{cutoff}}$  is decreased. The maximum temperature obtained for any combination of  $\gamma_1$  and  $\gamma_2$  is reached when  $\alpha_{\text{cutoff}} = 0.26^\circ$ , or when thermal emission is limited to the same solid angle that light is received from the sun. Here also, we see that the temperature response is more sensitive to decreases in thermal emission into large angles, as opposed to increases in solar absorption near normal; hence, temperature depends more strongly on  $\gamma_2$  than  $\gamma_1$ . We note that in the ideal limiting case with  $\gamma_2 = 0$  the dependence on  $\alpha_{\text{cutoff}}$  corresponding to the darkest blue trace in Figure 2d is obtained for any value  $\gamma_1 \neq 1$ .

Unlike the wavelength selective absorber described above, increasing temperature using only angle selective absorption and emission requires that the correct orientation with respect to the optical source is maintained. For structures heated by sunlight, this can be achieved with mechanical solar trackers that move the absorber to follow the sun over the course of the day and

year. Similar strategies are employed in solar-thermal power converters and photovoltaic schemes that use external lenses or optical concentrators to increase the intensity of sunlight on the converter, since lenses also require correct orientation. Indeed, restricting angle dependent emission as described here provides the same temperature increases that can be achieved using optical concentrators, because concentrator lenses effectively increase the solid angle of radiation received from the sun, increasing the angle range of the integral describing the power balance in eq 5. The net effect is equivalent to decreasing the angle dependent emission in eqs 6 and 8. Note that lenses also increase the apparent power from sunlight hitting the absorber, based on the concentration factor of the lens. This dependence on angle range is why the two strategies, concentrator optics or angle restrictive emission, have little theoretical benefit if used in conjunction. However, unlike conventional concentrator lenses, selective absorbers can be designed to have high absorption of sunlight at all angles but low emission of thermal radiation into any angle, as we outline below. Thus, nanostructured surfaces can provide many advantages in comparison with conventional tracking optics used in solar-thermal concentrator applications.

## ■ PLASMONIC ABSORBER DESIGN

With knowledge of the ideal absorption and emission properties that can give rise to the largest temperature increases during photothermalization of direct sunlight, we next show how the spectral and angle dependent emissivity of plasmonic surfaces can be engineered to approximate this ideal response. We are particularly interested in what temperatures can be reached under direct sunlight, for potential application in a variety of solar energy conversion schemes that take advantage of plasmonic heating.<sup>19,23</sup> Further, we show below how maximizing the lattice temperature of the metal is a crucial step for also increasing the temperature of the non-equilibrium hot electrons during steady state absorption.

Several design motifs among researchers in plasmonics and nanophotonics have been established that use periodic subwavelength arrays to provide desirable optical attributes, such as strong broadband absorptivity, restricted angular emission, or thermal energy beaming.<sup>36–38</sup> In our studies, we assess a proposed absorber design and then model the optical and thermal response iteratively, modifying design parameters until the highest predicted temperature is obtained. Full wave electromagnetic simulations (finite difference time domain method) using commercially available software (Lumerical) allow us to determine  $\alpha(\lambda, \theta, \phi)$ . Based on this emissivity function and eqs 3–8, we then calculate the anticipated temperature when the plasmonic array is placed in direct sunlight, assuming negligible  $P_{\text{nonradiative}}$ . A simple but effective example geometry of a cubic array of Au nanoscale cylinders on a Au substrate is depicted in Figure 3a. Here, the periodicity and cylinder dimensions were varied systematically to identify the geometry that provided the highest predicted temperature during solar absorption, giving  $T = 1119$  K. For reference, the melting temperature of bulk Au is 1336 K.<sup>39</sup> We observe several features in the emissivity function that provide this large temperature, as summarized in Figure 3b,c. Near-unity broadband emissivity is maintained throughout the visible spectrum for wavelengths below  $\lambda_{\text{cutoff}} = 590$  nm. Further, this strong emissivity is largely insensitive to incident angle, as indicated by the integrated emissivity over the entire hemisphere of incident angles, Figure 3b. Finally, low emissivity is maintained over all angles for wavelengths larger than  $\lambda_{\text{cutoff}}$ , thus approximating

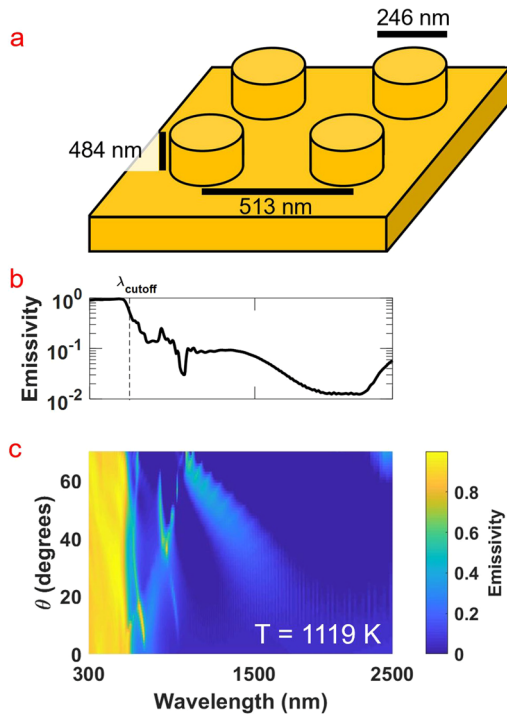


**Figure 3.** (a) Schematic geometry of a Au nanostructure with the corresponding simulated emissivity function (b) integrated over the entire hemisphere of surface emission to show the wavelength cutoff at 590 nm, as well as (c) the explicit dependence on zenith angle ( $\theta$ ).

many of the desirable features outlined in Figures 1 and 2. As discussed in more detail below, a structure with a lattice temperature that is as close as possible but below the melting point also allows for the maximum possible increase to the electronic temperature, without destruction of the absorber due to melting.

### MEASURING LATTICE TEMPERATURE AND ELECTRONIC TEMPERATURE IN THE STEADY STATE

In order to quantify the actual temperatures that are obtained via photothermalization, gold nanostructures were fabricated using electron beam lithography, as outlined in the *Methods section*. A schematic and SEM image of a fabricated array of nanoscale

cylinders deposited on a 100 nm thick Au film, with features comparable to the modeled structure in Figure 3, are depicted in Figure 4a,b. The temperature of the metal during optical absorption was determined by an analysis of an anti-Stokes Raman signal that resulted from optical excitation of the pure metal sample. Full details of the fitting routine employed for the temperature analysis and a discussion of the physical origin of this Raman signal are described below. The Raman signal was collected during illumination with a 532 nm continuous wave (CW) laser across incident powers spanning  $8 \times 10^8$  to  $9 \times 10^9$  W/m<sup>-2</sup>. This laser also served as the optical source that heated the nanostructure via absorption and photothermalization. A representative data set is shown in Figure 4c. As incident optical power increases, the anti-Stokes signal increases monotonically. At higher fluences, greater than  $4 \times 10^9$  W/m<sup>-2</sup>, there is the appearance of two peaks in the spectra at  $-1350$  and  $-1580$  cm<sup>-1</sup> which indicate the formation of amorphous carbon on the surface of the gold. This amorphous carbon signal is commonly observed at high optical fluences in SERS and in tip-enhanced Raman spectroscopy (TERS) experiments, and it likely results from the photodegradation of trace amounts of organic contaminants that are adsorbed to the metal surface during measurement.<sup>40,41</sup> Data in this wavenumber range is excluded during analysis to prevent artifacts that are not attributed to the gold surface from interfering with the fitting routine. The signal collected from a gold film control sample was  $\sim 10\times$  weaker than the signal from a nanostructure at equivalent incident optical power, consistent with enhancements commonly seen in SERS measurements.<sup>1</sup>

Scattering by phonons does not contribute to the Raman signal observed from pure metals.<sup>42</sup> Rather, the broad signal is due to a direct interaction with the electron gas and therefore provides information about the energetic distribution of the electrons.<sup>18</sup> Recent studies suggest this signal may be due to anti-Stokes photoluminescence from the recombination of the short-lived photoexcited electron–hole pairs in the metal, rather than a coherent scattering process, as with conventional Raman spectroscopy of vibrational modes.<sup>18,43</sup> However, the exact physical origin of the anti-Stokes signal is still under debate and may be dependent on the specific metal or nanoscale geometry under study.<sup>43</sup> Despite uncertainty about the physical mechanism, it has been well established that this anti-Stokes signal is a reliable reporter of the lattice temperature of the

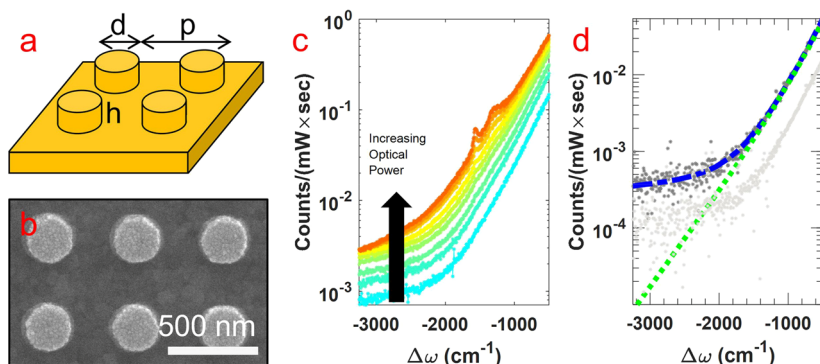


**Figure 4.** (a) Schematic of a Au nanostructure with dimensions  $h = 100$  nm,  $p = 500$  nm, and  $d = 273$  nm and (b) the corresponding SEM image. (c) The power dependent anti-Stokes Raman signal, with the growth of amorphous carbon peaks around  $-1500$  cm<sup>-1</sup> at higher powers. The power range spanned is  $8 \times 10^8$  to  $9 \times 10^9$  W/m<sup>-2</sup>. (d) A one-temperature fit ( $T = 505$  K, green dotted) and the two-temperature fit ( $T_1 = 456$  K,  $T_e = 5523$  K, and  $\chi = 1.01\%$ , blue dashed) for an incident optical power of  $4.2 \times 10^8$  W m<sup>-2</sup>. The weaker signal (light gray dots) is from a smooth Au film.

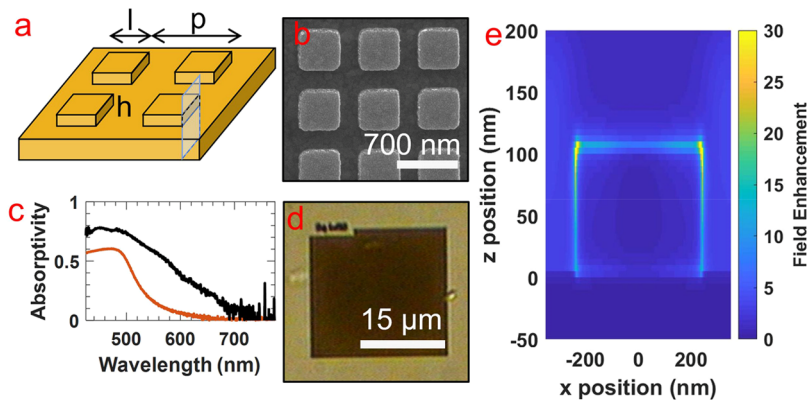


**Figure 5.** (a) Schematic of a periodic structure with strong optical field enhancement for enhancing Raman signal, with  $l = 225 \text{ nm}$ ,  $p = 500 \text{ nm}$ , and  $h = 100 \text{ nm}$  on a  $150 \text{ nm}$  thick gold film. (b) SEM and (d) optical image of the fabricated nanostructure. (c) The absorptivity at normal incidence of the nanostructure (black) compared to a smooth gold thin film with a thickness of  $150 \text{ nm}$  (red). (e) The calculated optical field enhancement on a side face of a nanocube, as depicted in part a. A maximum field enhancement of  $47\times$  at the corners is predicted.

metal.<sup>17,18,44</sup> Thus, the Bose–Einstein distribution of the phonon excitations describes the spectral trend:

$$I(\Delta\omega) = C \times D(\Delta\omega) \times \left( \frac{1}{e^{(hc\Delta\omega/kT_l)} - 1} \right) \quad (9)$$

Here,  $I$  is the anti-Stokes signal normalized by power and integration time as a function of the energy difference from the Rayleigh line,  $\Delta\omega$ , and the lattice temperature,  $T_l$ . To account for the experimental collection efficiency, a scaling factor,  $C$ , is included that is calibrated for each measurement. The density of states of the material,  $D(\Delta\omega)$ , is obtained experimentally from a reflection spectrum.

When fitting our data to eq 9, as plotted in Figure 4d (green dotted line), we find that the spectrum is described very accurately near the Rayleigh line but deviates significantly at Raman shifts greater than  $-2000 \text{ cm}^{-1}$ . This deviation at high energy shifts has been observed throughout SERS and TERS studies during CW excitation.<sup>18,40,45</sup> Recent reports, including a study from our lab, attribute this high energy signal to the presence of a sustained subpopulation of hot electrons in the metal that are at an elevated temperature in comparison with the majority electron bath.<sup>29,40</sup> Importantly, as we show below, this interpretation can be verified independently in a thermionic device geometry that measures the temperature and size of the hot electron subpopulation based on the electrical signal of vacuum emitted electrons. A consistent physical picture that explains the Raman signal is as follows. First, after optical absorption, photoexcited electrons quickly exchange energy with other hot electrons via electron–electron scattering ( $\sim\text{fs}$ ) to establish a distinct electronic subpopulation with a well-defined temperature,  $T_e$ . Then, on a longer time scale ( $\sim\text{ps}$ ), hot electrons within the subpopulation equilibrate with the rest of the electron bath at a rate determined by electron–phonon scattering, to achieve a distribution at temperature  $T_l$ . During illumination, some steady state population of hot electrons will always be present that is defined by the optical absorption rate as well as the magnitude of the electron–phonon coupling. Adapting the fitting method of Szczerbiński et al., we find that the additional signal at higher wavenumbers can be accounted for by including an additional term to describe the relative size of the subpopulation of hot electrons,  $\chi$ , with temperature  $T_e$ .

$$I(\Delta\omega) = C \times D(\Delta\omega) \times \left( \frac{1 - \chi}{e^{(hc\Delta\omega/kT_l)} - 1} + \frac{\chi}{e^{(hc\Delta\omega/kT_e)} + 1} \right) \quad (10)$$

Carriers in equilibrium probe the phonon distribution and therefore show the Bose–Einstein statistics of lattice excitations, while the hot electron subpopulation is described by Fermi–Dirac statistics.<sup>46</sup> We note that spectra can also be well described assuming that the hot electron population obeys Boltzmann statistics, and both distributions provide similar values for the fitted parameters. The fit to eq 10 is also plotted in Figure 4d (blue dashed) and shows excellent agreement with the data over the entire spectral range. Moreover, this analysis accurately describes spectra measured over a wide range of optical powers from  $10^6$  to  $10^{11} \text{ W m}^{-2}$  in our experiments.<sup>29</sup> We also emphasize that the Raman signal we attribute to the hot electrons is very weak compared to the signal from the thermalized electron bath, especially for thin film samples without SERS enhancement. As understood in an expanded TTM model, it is also expected that some contribution to the signal is from nonthermalized electrons. However, based on the optical power densities probed in our experiments, we believe that the average time between photon absorption events is greater than the time scale of electron–electron scattering. Thus, there is not a significant fraction of the electron population corresponding to the nonthermal component prevalent in our spectra, or  $\ll 1\%$ . In experiments, it is crucial to eliminate sources of error and other artifacts such as stray lights or unwanted scattering. Additionally, long integration times of several minutes and a rigorous procedure for assessing the spectral baseline are required to obtain data that can be fitted robustly. We also cannot fully discount other small effects contributing to the signal, such as shifts in the plasmon resonances of the nanostructures due to volume expansion during heating. Nevertheless, the electrical device data we report below confirms major trends in the behavior of the hot electrons that are also consistent with the interpretation of the Raman spectra in accordance with eq 10.

The large increase in Raman signal from the nanostructured film compared to a smooth Au film in Figure 4d is due to the large optical field enhancement provided by the plasmon resonance of the nanoscale cylinders. Given the importance for

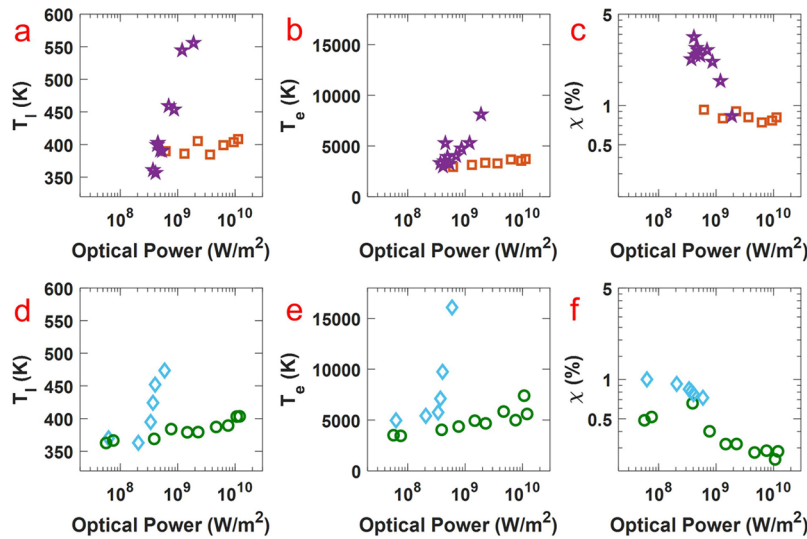


**Figure 6.** (a–c) The fitted values of  $T_l$ ,  $T_e$ , and  $\chi$ , respectively, for a 150 nm thick gold film measured in the atmosphere (red squares) and in a vacuum (purple stars) as a function of incident optical power. (d–f) The fitted  $T_l$ ,  $T_e$ , and  $\chi$ , respectively, for the gold nanostructure in Figure 5d, measured in the atmosphere (green circles) and in a vacuum (blue diamonds).

maximizing the Raman signal to aid interpretation of the electronic and lattice temperature in systematic temperature studies, we turn to a substrate design that will maximize local field enhancements, similar to the design of SERS substrates. It is well established that optical field concentration is strongest at corners and sharp tips in plasmonic absorbers.<sup>47</sup> Indeed, a nanocube array shows very high field enhancement at corners, as shown in schematically in Figure 5a along with corresponding optical and SEM images (Figure 5b,d). With proper tailoring of this geometry, highly absorbing structures can be made that also approximate the selective absorber behavior observed in the pillar geometry in Figure 3. Again, using full wave optical simulations (FDTD method), we determine an optimized periodic structure that provides strong broadband absorption and high local field enhancement. As depicted along one face (Figure 5e), the nanocube shows nearly 50× field enhancement at the sharp corner compared with the incident optical intensity. The fabricated structure also exhibits strong, broadband absorption in the visible (Figure 5c).

Using fits to the anti-Stokes Raman signal, we track the dependence of  $T_l$ ,  $T_e$ , and  $\chi$  on optical power for the optimized absorber in Figure 5 and compare the response with a smooth 150 nm thick Au film. Both samples were fabricated on a silicon wafer substrate. The results from the study of the Au film, with the fitted  $T_l$ ,  $T_e$ , and  $\chi$ , are displayed in Figure 6a–c, respectively. Due to the weaker Raman signal compared with the nanostructure array, temperatures can only be robustly fitted for spectra obtained at a minimum incident laser power of  $5 \times 10^8$  W m<sup>-2</sup>, corresponding to a significant temperature increase in both  $T_l$  and  $T_e$ . Note that above a measured  $T_l$  of 600 K we observe the onset of thermal degradation of samples, further limiting the power range that can be measured. Based on eq 7, the highest lattice temperature an absorber can reach is limited by the magnitude of the  $P_{\text{nonradiative}}$  term, due to effects such as convection or conduction. In order to understand the role of convection, we performed anti-Stokes Raman measurements both in the atmosphere and at a vacuum pressure of 0.010 mbar. Indeed, placing the gold film in a vacuum significantly increases the  $T_l$  that was obtained during absorption, though the sample substrate also provided a conduction pathway of thermal energy

away from the sample, significantly limiting the photothermal response. Perhaps more striking is the very large dependence of  $T_e$  on the vacuum pressure, with electronic temperatures in the vacuum exceeding those in the atmosphere by as much as a factor of 4. This suggests that electronic temperature is also highly dependent on nonradiative loss pathways. It has been well established that gold nanostructures can interact with surface adsorbed molecular species in a process known as chemical interface damping (CID).<sup>48,49</sup> During CID, direct photoexcitation into adsorbate states decreases the plasmon lifetime by introducing another pathway by which it can decay. Given that we see the formation of amorphous carbon under high illumination, there is strong evidence that photoexcited electrons are interacting with adsorbed molecules from the atmosphere either through CID or hot electron injection. Further, an observed decrease in  $T_e$  and  $\chi$  is consistent with plasmon damping due to CID. A more detailed analysis of both the hot electron lifetime and electron–phonon coupling is provided below, giving more insight into the nature of electron relaxation pathways.

Moreover, there is a monotonic increase in temperature with increasing laser power, with the magnitude of electronic temperature in both the atmosphere and the vacuum exceeding the lattice temperature by well over an order of magnitude. This is expected due to the  $\sim 100\times$  smaller heat capacity of the electron gas compared to the lattice,<sup>16</sup> and this difference between electronic and lattice temperature has also been observed in TA studies.<sup>40,45,50</sup> Interestingly, we find that in both environments there is an inverse relationship between the trend in  $T_e$  and  $\chi$  as the optical intensity is increased, though the trend is more pronounced when the thin film is in a vacuum. It has also been established in TA studies and computational studies that there is an increase in electron–phonon coupling as electronic temperature increases, resulting in faster rates of electron relaxation.<sup>51</sup> We similarly interpret the observed trend in  $\chi$  as resulting from an increase in the rate of hot electron relaxation with temperature that outcompetes the increase in the excitation rate of hot electrons at higher laser fluences.

An analysis of the nanostructure array described in Figure 5 with the fitted values of  $T_l$ ,  $T_e$ , and  $\chi$  is displayed in Figure 6d–f,

respectively. A benefit of measurements performed on nanostructures is that the field enhancement provides an increase in signal, allowing more reliable spectra at lower optical powers and decreased noise. Both in the atmosphere and under a vacuum,  $T_l$  and  $T_e$  are larger in comparison with the gold film at equivalent optical power, due to the increase in absorbance. However, the onset of thermal degradation occurred at somewhat lower lattice temperatures in a vacuum compared with the gold film, limiting the high power range of the study. Even still, the electronic temperatures reached are nearly twice as high as the gold film at the highest optical powers. Additionally, the nanostructure array shows the same inverse relationship between  $T_e$  and  $\chi$ . The much higher electronic temperatures entail that the nanostructures exhibit a relatively smaller subpopulation of hot electrons at the same optical powers compared with the film. However, for equivalent values of  $T_e$ , the nanostructure exhibits a larger  $\chi$  than the thin film, when the samples are in the atmosphere. Again, this can be interpreted as resulting from changes in the electron–phonon coupling that depend on environmental factors and geometry and is described in detail in the discussion below.

With the insight provided by the anti-Stokes Raman analysis, it is possible to adapt the traditional two-temperature model given in eq 1 in order to account for the steady state behavior of the metal when it is absorbing optical power,  $P_{abs}$ . Crucially, the expression now includes a specific dependence on the size of the hot electron subpopulation,  $\chi$ . In eq 1, both  $\frac{\partial C_e T_e}{\partial t}$  and  $G(T_e - T_l)$  refer to heat-transfer rates between different subpopulations in the material, and both are extensive quantities that are scaled by  $\chi$  in order to accurately describe the amount of electrons participating in the thermalization process. Further,  $T_e$  refers only to the temperature of electrons within the hot electron subpopulation:

$$\chi C_e \frac{\partial T_e}{\partial t} = \nabla[k_e \nabla T_e] - \chi G(T_e - T_l) + P_{abs} \quad (11)$$

In the steady state, the time derivative goes to zero, allowing a description for  $T_e$  in terms of the lattice temperature of the system,  $T_l$ , as can be obtained from eqs 3–8 above. If we neglect local thermal gradients, then

$$T_e = T_l + \frac{P_{abs}}{\chi G} \quad (12)$$

We see that the electronic temperature is greater than the lattice temperature by an additional term that accounts for the power absorbed and the electron–phonon coupling constant,  $G$ . Further, increases in electronic temperature are expected to correlate with decreases in  $\chi$ , as observed in Raman measurements. If the electron–phonon coupling observed in ultrafast TA studies is also representative of electron dynamics in this regime of steady state absorption, we can make specific predictions about how electronic temperature depends on lattice temperature. Assuming  $\chi$  of 1%, a conservative estimate based on the data measured in Figure 6, and assuming a  $G$  value of  $10^{13} \text{ W m}^{-3} \text{ K}^{-1}$ , based on calculated and reported values for nanoscale gold,<sup>46</sup> when a Au thin film is absorbing solar illumination, eq 12 predicts that the steady state temperature difference between lattice and electronic temperature is only a few degrees. However, all three terms that define the increase in electronic temperature with respect to lattice temperature,  $\chi$ ,  $G$ , and  $P_{abs}$ , appear to be modified by the geometry of the nanoscale absorber in our studies. In the first half of this report, we

demonstrated how to design a nanostructure that has optimized absorption for maximizing  $T_l$  and  $P_{abs}$  which leads to an increase in  $T_e$ , as calculated by eq 12. Another consequence of a careful choice of geometry is that optical absorption can be strongly enhanced at electromagnetic hot spots, thus effectively increasing  $P_{abs}$  locally even further in the structure, sometimes by orders of magnitude compared with the incident optical intensity, depending on the nanoscale geometry. Further, in addition to the trends in  $\chi$ , that depend on optical power and environment as reported above, we will show how structural features in the nanoscale absorber relate to the size of  $\chi$  and the electron–phonon coupling constant,  $G$ , as determined by Raman measurements, thereby also providing new insight into the factors that determine the rate at which electrons thermalize with the bath. Therefore, the hot electron temperature than can be sustained in the steady state is informed by systematic analysis of the anti-Stokes Raman signal, in combination with more well-established design considerations for locally enhancing optical fields.

## ■ VERIFICATION OF THE HOT ELECTRON SUBPOPULATION: THERMIONIC DEVICES

It is important to emphasize the distinct features of the steady state TTM model and the corresponding physical picture provided by the anti-Stokes Raman analysis, in comparison with the traditional TTM from TA studies. In particular, it is not usually suggested in TA studies that the electron population in the metal can be separated into two separate populations, each with well-defined temperatures. Rather, in time-resolved experiments, it is believed that after an optical pulse all conduction electrons in the metal thermalize through electron–electron scattering to reach a uniform elevated temperature, before thermalizing with the lattice via electron–phonon scattering. Second, the Raman signal indicates a fractional size of the population of hot electrons that seems incredibly large, especially in light of the very short (~ps) lifetime of photoexcited electrons. That said, the high energy tail of the anti-Stokes Raman spectra is clear in many other reports,<sup>18,40</sup> and our lab and others have consistently presented evidence for sustained hot electron populations on the order of ~1%, with temperatures >1000 K during optical pumping across similar intensities.<sup>29,40</sup> Given the ongoing debate in the field about the fundamental physical mechanism that gives rise to the anti-Stokes Raman signal from metal, clearly it will be necessary for many more studies to shed light on the full dynamics of the electron gas that connect these disparate regimes of CW and time-resolved experiments.

However, we provide a distinct physical characterization method that indicates the existence of the hot electrons, their temperature, and other power dependent trends lending credence to the steady state TTM summarized in eq 10. We have developed a technique to measure the hot electrons directly by constructing a thermionic converter device.<sup>29</sup> A thermionic converter is an electrical device in which a metal cathode is heated to a high temperature (greater than thousands of K) so that some electrons in the cathode have kinetic energy in excess of the work function,  $W$ . These electrons are emitted across a vacuum gap and collected at an anode. Instead of conventional heating, we fabricate a cathode that is plasmonically structured to be highly absorbing, so that optical excitation induces heating via photothermalization. If the incident radiation has insufficient energy to promote direct photoemission via the photoelectric effect, i.e.,  $h\nu < W$ , then the electrical signal due to vacuum

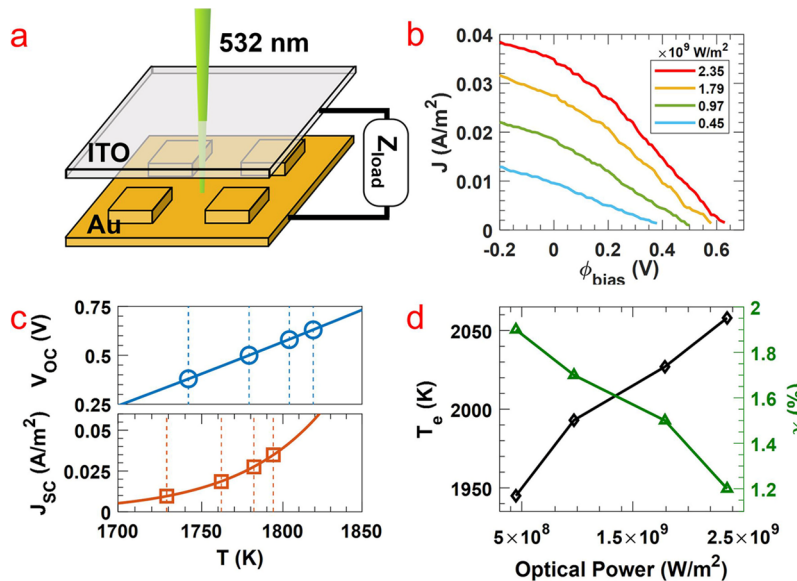


**Figure 7.** (a) A schematic of the thermionic device composed of a Au nanostructure and ITO-coated glass slide. (b) The measured  $J$ – $V$  curves as a function of incident optical power. (c) The fitted temperatures calculated assuming a one-temperature model based on  $V_{OC}$  (top) or based on  $J_{SC}$  (bottom). (d) The fitted trend in  $T_e$  and  $\chi$  solved using a two-temperature model.

emission provides information about the energetic distribution of the electrons in the cathode. Importantly, the electrons need to be at extremely elevated temperature to observe any thermionic signal, and neither our anti-Stokes Raman analysis or other experiments<sup>52</sup> suggest that optical excitation can provide increases in the lattice temperatures of metals that would support thermionic emission, especially without inducing melting or vaporization of the metal.

We constructed a thermionic device using the Au nanostructure depicted in Figure 5 as the cathode with an ITO anode separated by 200  $\mu\text{m}$  and placed the device under a vacuum (0.010 mbar). The sample was excited with 532 nm CW laser excitation, and the electrical signal was measured using lock-in amplification, as depicted in Figure 7a. The current–voltage ( $J$ – $V$ ) response of the device is shown in Figure 7b. As laser power is increased, there is an increase in both the measured short circuit current,  $J_{SC}$ , as well as the open circuit voltage,  $V_{OC}$ . Note that, because the ITO anode provides no reverse thermionic current in the experiment, the current exponentially approaches zero against an increasing bias. Therefore, the reported  $V_{OC}$  corresponds to the maximum applied voltage that still allowed lock-in detection of the current. Given that the lattice temperature of the metal is too low to provide any electrons with kinetic energy sufficient for vacuum emission, we interpret the electrical signal as resulting only from the hot electrons in the cathode. The electrical signal can be understood in terms of the Richardson equation for thermionic emission, which we have adapted to account for the steady state TTM model.<sup>29</sup>

$$J = \chi A T_e^2 e^{-(W + \phi_{bias} + \phi_{sc})/kT_e} \quad (13)$$

This equation relates the thermionic current density,  $J$ , to a retarding applied voltage,  $\phi_{bias}$ , taking into account the work function of Au,  $W = 5.1$  eV<sup>53</sup> and the Richardson constant,  $A$ . It is also necessary to include a term to account for the space charge potential in the vacuum gap,  $\phi_{sc}$ , which we estimate from Langmuir's space charge theory for a parallel plate geometry.<sup>54</sup> We assume that only the fraction of electrons in the metal,  $\chi$ , at

the hot electron temperature,  $T_e$ , give rise to the vacuum emission. Removing the dependence on  $\chi$  and assuming that all electrons and the lattice are at one uniform temperature,  $T$ , reproduces the standard Richardson equation.

This expression connects the  $J$ – $V$  characteristics of the device with the temperature and population of the hot electrons in the cathode, and an analysis of the trends in  $V_{OC}$  and  $J_{SC}$  indicates that a TTM is required to accurately describe the electrical data. As summarized in Figure 7c, there is a discrepancy in the fitted temperature based on the  $J_{SC}$  compared with the temperature fit by analysis of the  $V_{OC}$ , if it is assumed that the entire electron gas is at a uniform temperature. However, for any incident optical power, there is a unique combination of  $\chi$  and  $T_e$  that consistently reproduces the trends in  $J_{SC}$  and  $V_{OC}$  when input into eq 13. In Figure 7d, we report these values and see that the electrical data shows the same inverse relationship between  $T_e$  and  $\chi$ , in agreement with the trends observed during the anti-Stokes Raman analysis of the same nanostructure array. Additionally, both  $\chi$  and  $T_e$  are approximately the same order of magnitude as that measured by the different techniques, though the fitted electrical data indicates a somewhat lower value of  $T_e$  than the Raman studies at comparable optical power. We believe that difficulties in accurately modeling the more complex space charge field of the nanostructure array may be the largest source of the discrepancy between the fitted values for  $T_e$  in the separate experiments. A more detailed discussion of the design, characterization, error analysis, and use of similar thermionic devices, especially for application in solar energy conversion, is provided in a separate report from our lab.<sup>29</sup> Moreover, the fundamental features of the steady state TTM consistent with the Raman data, relating the size and the temperature of a sustained subpopulation of hot electrons, are also indicated by the behavior of the plasmonic thermionic devices.

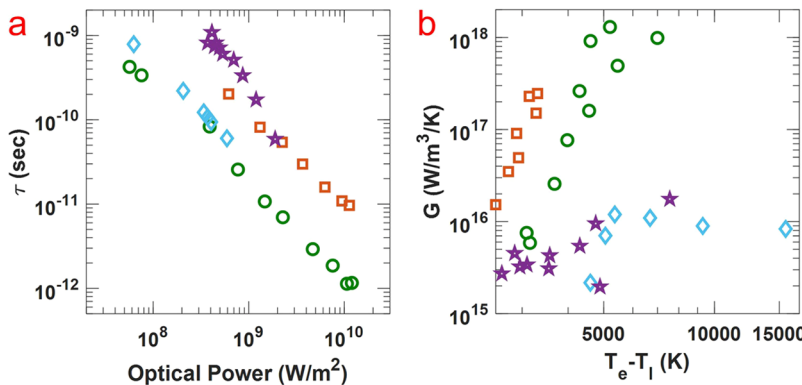


**Figure 8.** (a) Calculated lifetime and (b) coupling constant for the nanostructure under a vacuum (blue diamonds), the nanostructure in the atmosphere (green circles), a gold thin film under a vacuum (purple stars), and a gold thin film in the atmosphere (red squares).

## ELECTRON-PHONON COUPLING AND THE HOT ELECTRON LIFETIME

With greater confidence that the anti-Stokes Raman spectra provide information that is descriptive of the steady state behavior of the hot electrons, we show how the Raman data summarized in Figure 6 can be further analyzed to provide detailed information about both the electron–phonon coupling constant,  $G$ , and a quantity,  $\tau$ , that indicates the average lifetime an excited electron resides in the hot electron subpopulation. The average lifetime of hot electrons within the elevated temperature distribution can be understood by comparing the size of the steady state subpopulation of hot electrons with the rate of hot electron generation. If it is assumed that every absorbed photon produces a transiently excited electron, then

$$\tau = \frac{\chi\rho V}{N\alpha} \quad (14)$$

where  $\rho$  is the electron density of gold,<sup>55</sup>  $V$  is the volume of the metal interacting with the light,  $N$  is the incident number of photons per second,  $\alpha$  is the experimentally measured absorptivity at normal incidence at 532 nm, and  $\chi$  is the fractional hot electron population from the anti-Stokes Raman fit. The interaction volume in our calculations is based on an estimate of where the absorption is localized in the nanostructures, as determined from optical simulations, similar to the depiction in Figure 5e. However, the actual interaction volume in the nanostructures is a complicated function of the local field concentration provided by the plasmonic resonances, and this may be a source of a systematic offset in the reported values for  $\tau$  below. As can be seen in Figure 8a, for all four data sets, there is a monotonic decrease in  $\tau$  as the incident optical power is increased. This decrease in the lifetime with optical power can be interpreted as resulting from thermal activation of the rate of coupling between the hot electrons and the lattice, as discussed above. This interpretation is further supported by the analysis of the electron–phonon coupling constant that follows. Further, samples under a vacuum show significantly longer  $\tau$  than those at atmospheric pressure. We hypothesize that this difference may be due to surface collisions with gas molecules or adsorbed contaminants in the atmosphere. The observation of the formation of amorphous carbon at higher optical power provides further evidence that electrons interact with surface species during illumination. With careful experimental design, trends in lifetime and hot electron population may allow these measurements to further distinguish mechanisms of hot electron injection or CID.<sup>40,48,49</sup>

However, what is very striking is the large range of  $\tau$  observed, spanning 3 orders of magnitude. Remarkably, our data suggests that at the lowest optical powers studied the hot electrons have high kinetic energy for nearly a nanosecond before thermalizing to the lattice temperature. At the highest optical powers, more directly comparable to the optical intensities employed in ultrafast TA studies, we see values for  $\tau$  that are very similar to the lifetime values of 1–10 ps that are standardly reported for Au.<sup>56,57</sup> While the comparison between the separate experiments is interesting, we caution that more insight is required to fully interpret this data. In particular, the strong field concentration at electromagnetic hot spots may entail that hot electrons absorb photons multiple times before relaxing, thereby increasing their average lifetime during steady state excitation. As confirmed in the electrical measurements above, the large, sustained population of energetic hot electrons provided by the prolonged lifetime is advantageous for their application in technology. However, if optical fluence is decreased further, below our detection limits in this study, the time between photon absorption events will begin to exceed the lifetime of hot electrons established in TA measurements, and therefore, the lifetime may show a more complex dependence on decreasing power.

Further analysis of  $\chi$  allows us to determine the electron–phonon coupling constant,  $G$ , independently from the lifetime, shown in Figure 8b. As described in eq 12, all of the fit parameters from the anti-Stokes Raman analysis allow unique determination of  $G$ , based on the absorbed power into volume of the metal interacting with the incident light. Unlike the analysis for lifetime, calculation of  $G$  requires quantification of the volumetric power absorbed,  $P_{V,\text{abs}}$ , in terms of the incident power,  $P_{\text{incident}}$ . Thus,  $P_{V,\text{abs}} = \frac{P_{\text{incident}} \times \alpha(\text{normal, 532 nm})}{V}$ . We have shown that at atmospheric pressure there are significant environmental contributions to the hot electron lifetime, implying that  $G$  accounts for coupling to all relaxation pathways. However, in a vacuum, it is expected that electron–phonon coupling will dominate relaxation. For all samples, there is an increase in  $G$  as a function of the electronic temperature, in agreement with *ab initio* calculations and experimental studies.<sup>51</sup> Notably, in the atmosphere, the gold thin film exhibits a larger  $G$  than the nanostructure at the same optical power. In a vacuum, the environmental influences are minimized, and within the spread of the data, the nanostructure and thin film show an equivalent coupling constant that agrees with calculated values for gold.<sup>57–59</sup> We hypothesize this trend in  $G$  is due to a decrease

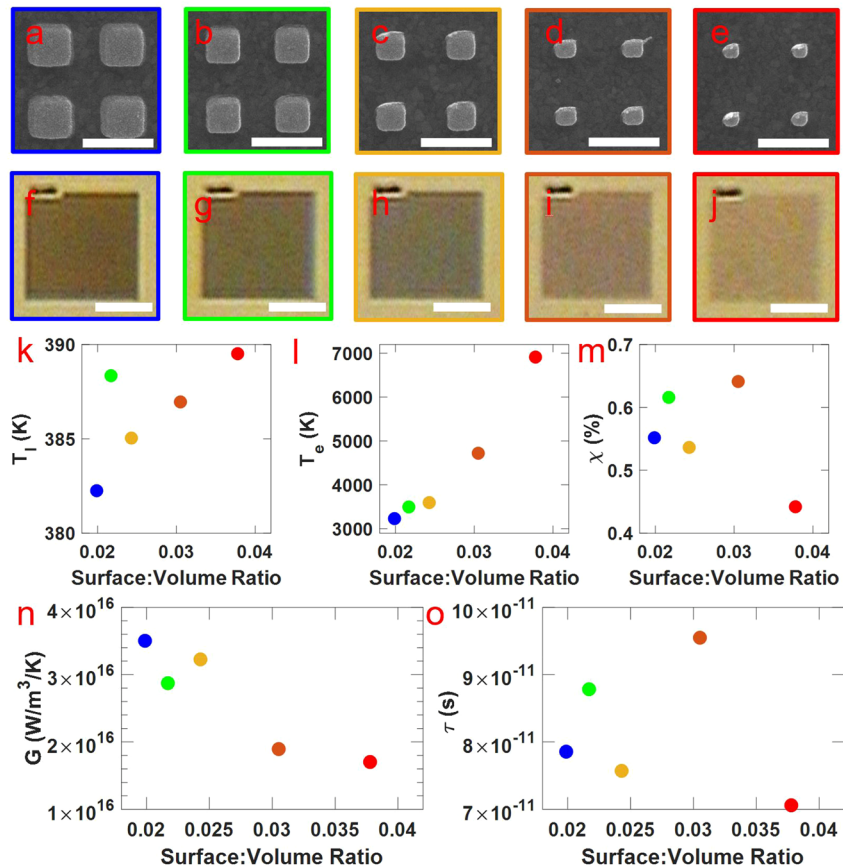


**Figure 9.** (a–e) SEM images of gold nanostructures with a constant pitch of 700 nm, a height of 100 nm, and an edge length of 470, 400, 340, 280, and 200 nm, respectively. The scale bar is 700 nm in each SEM image. (f–j) Optical images of each nanostructure in parts a–e; all scale bars are 15  $\mu\text{m}$ . As a function of surface:volume ratio, for the five nanostructures, we show  $T_l$  (k),  $T_e$  (l),  $\chi$  (m),  $G$  (n), and  $\tau$  (o).

in the active surface area with hot electrons, likely localized near electromagnetic hot spots, and that only molecule collisions in these locations contribute to relaxation. The net result is that the nanostructure achieves much greater  $T_e$  under equivalent optical power, and further, hot electrons have longer lifetimes compared with thin films at the same  $T_e$  in the atmosphere. Both behaviors may be desirable in devices that take advantage of hot electrons, and our results suggest optical designs that decrease the relative volume in which hot electrons are generated can further optimize this response.

Given this observed dependence on the geometry of the nanostructure, we have also performed a systematic analysis of the parameters  $T_l$ ,  $T_e$ ,  $\chi$ ,  $G$ , and  $\tau$ , as a function of the surface to volume ratio of periodic arrays of gold nanocubes, shown in SEM in Figure 9a–e and optically in Figure 9j–f, illuminated in the atmosphere. The period was maintained across samples, and the incident power on each sample was modulated by the relative absorption cross section, so that  $2.1 \times 10^8 \text{ W m}^{-2}$  optical power was equivalently absorbed by all arrays during steady state excitation. Because the same optical power was absorbed by each array, the trends observed give clear insight into how geometry alone affects hot electron behavior. The fit to parameters  $T_l$ ,  $T_e$ ,  $\chi$ ,  $G$ , and  $\tau$  are depicted in Figure 9k–o, respectively. We find an increase in  $T_l$  and  $T_e$  with increasing surface to volume ratio. Equivalently, smaller nanostructures reach higher temperatures when absorbing the same optical power. As above,  $T_e$  is systematically larger than  $T_l$ . Increases in the electronic temperature may also be correlated with a decrease in the hot electron population,  $\chi$ , as reported above. However, as with the

trend in lifetime,  $\tau$ , interpretation of the signals in Figure 9m and o is difficult due to the spread in the data and may be effectively constant across the size range of samples studied. As predicted, we also find that the coupling constant,  $G$ , decreases with increasing surface to volume ratio. This indicates that smaller nanostructures provide better isolation from environmental factors that accelerate the relaxation of hot electrons. In combination with the increase in  $T_e$ , these results suggest that applications taking advantage of hot electrons may need to trade off the higher electronic temperature provided by the more localized hot spots in smaller structures, against better access to hot electrons produced in larger structures with less localization.

## SUMMARY AND OUTLOOK

Our report has given comprehensive information about the factors that control both the lattice and electronic temperature, as well as the availability of non-equilibrium hot electrons during steady state illumination. Optical excitation with CW, low intensity light is especially of interest as applications of hot electrons expand to broad classes of energy conversion devices and chemical reactions that may be powered by dilute or concentrated sunlight. Building from a comprehensive discussion of how nanostructured plasmonic materials can be engineered to reach the highest possible lattice temperatures, and therefore the highest possible electronic temperatures when exposed to sunlight, our results also inform how the hot electrons inside these materials can be understood and

controlled with increasing sophistication through modifications of nanostructure geometry.

Specifically, our experiments offer a new, detailed picture of the hot electron dynamics that characterize absorption in the steady state, based on careful analysis of anti-Stokes Raman spectra collected during photothermalization. Providing a complementary perspective of the hot electron dynamics that have been established from years of ultrafast time-resolved transient absorption studies, we find that plasmonic absorbers sustain a subpopulation of hot electrons at a significantly elevated temperature compared with the majority electron population that is thermalized with the metal lattice. Additionally, information about electron relaxation due to electron–phonon coupling and the remarkably long lifetime of hot electrons in the elevated temperature distribution can be learned from analysis of the Raman spectra. Importantly, we show how Raman measurements give predictive information for when hot electrons are employed in applications. We outline the specific case study of a thermionic converter based on hot electron emission. Finally, we also show how the geometry and the environment of a plasmonic absorber dictate the behavior of hot electrons, and thereby what may be an optimal application.

We believe that anti-Stokes Raman spectroscopy may become a powerful tool in the plasmonics and nanophotonics community for refining understanding of the photophysics and photochemistry that define applications of hot electrons. This is especially true, as the electron dynamics that the technique uncovers are fully reconciled with time-resolved experiments, and the next generation of computational studies further elucidates this remarkable behavior. We also believe that our experiments help further outline opportunities that will sustain interest in plasmonic hot electrons for years to come.

## AUTHOR INFORMATION

### Corresponding Author

\*E-mail: [sheldonm@tamu.edu](mailto:sheldonm@tamu.edu).

### ORCID

Shengxiang Wu: 0000-0002-1173-5569

Matthew Sheldon: 0000-0002-4940-7966

### Author Contributions

N.H. fabricated the plasmonic substrates and performed the Raman spectroscopy measurements. S.W. prepared and characterized the thermionic devices. The manuscript was written through contributions of all authors. All authors have given approval to the final version of the manuscript.

### Notes

The authors declare no competing financial interest.

## Biographies



William and Chris Jarvis

Nicki Hogan received her B.S. in chemistry from the University of West Georgia in 2015. She is currently pursuing a Ph.D. in physical chemistry at Texas A&M University under the supervision of Professor Matthew Sheldon. Her current research focuses on understanding hot electron dynamics in metallic nanostructures for thermionic applications.



William and Chris Jarvis

Shengxiang Wu, born in 1992, received his B.S. degree in chemical biology from Peking University in 2015. Now he is a Ph.D. candidate at Texas A&M University. His current work is on plasmonic “hot” carrier optoelectronic devices including “hot” carrier thermionic emission and tunneling.



William and Chris Jarvis

Matthew Sheldon received his B.A. from Carleton College (Chemistry) and Ph.D. from UC Berkeley (Chemistry), and he performed his postdoc at Caltech (Mat.Sci/App.Phys). He is the recipient of the 2015 Air Force Office of Scientific Research Young Investigator Program

(AFOSR YIP) Award and the Kaneka Junior Faculty Award (2017), and he was selected as a 2017 Inventor Fellow by the Gordon and Betty Moore Foundation. In 2019, he was elected to the executive committee of the American Physical Society (APS) Topical Group on Energy Research and Applications (GERA).

## ACKNOWLEDGMENTS

This work is funded by the Air Force Office of Scientific Research under Award No. FA9550-16-1-0154. M.S. also acknowledges support from the Welch Foundation (A-1886) and the Gordon and Betty Moore Foundation through Grant GBMF6882.

## REFERENCES

- (1) Cialla, D.; März, A.; Böhme, R.; Theil, F.; Weber, K.; Schmitt, M.; Popp, J. Surface-Enhanced Raman Spectroscopy (SERS): Progress and Trends. *Anal. Bioanal. Chem.* **2012**, *403*, 27–54.
- (2) Willets, K. A. Supercharging Superlocalization Microscopy: How Electrochemical Charging of Plasmonic Nanostructures Uncovers Hidden Heterogeneity. *ACS Nano* **2019**, *13*, 6145–6150.
- (3) Le Ru, E. C.; Etchegoin, P. G. Single-Molecule Surface-Enhanced Raman Spectroscopy. *Annu. Rev. Phys. Chem.* **2012**, *63*, 65–87.
- (4) Stewart, M. E.; Anderton, C. R.; Thompson, L. B.; Maria, J.; Gray, S. K.; Rogers, J. A.; Nuzzo, R. G. Nanostructured Plasmonic Sensors. *Chem. Rev.* **2008**, *108*, 494–521.
- (5) Padilla, W. J.; Basov, D. N.; Smith, D. R. Negative Refractive Index Metamaterials. *Mater. Today* **2006**, *9*, 28–35.
- (6) Vestler, D.; Shishkin, I.; Gurvitz, E. A.; Nasir, M. E.; Ben-Moshe, A.; Slobozhanyuk, A. P.; Krasavin, A. V.; Levi-Belenkova, T.; Shalin, A. S.; Ginzburg, P.; et al. Circular Dichroism Enhancement in Plasmonic Nanorod Metamaterials. *Opt. Express* **2018**, *26*, 17841–17848.
- (7) Litchinitser, N. M. Nonlinear Optics in Metamaterials. *Adv. Phys. X* **2018**, *3*, 1367628.
- (8) Link, S.; El-Sayed, M. A. Shape and Size Dependence of Radiative, Non-Radiative and Photothermal Properties of Gold Nanocrystals. *Int. Rev. Phys. Chem.* **2000**, *19*, 409–453.
- (9) Doughty, A.; Hoover, A.; Layton, E.; Murray, C.; Howard, E.; Chen, W. Nanomaterial Applications in Photothermal Therapy for Cancer. *Materials* **2019**, *12*, 779.
- (10) Wu, S.; Sheldon, M. T. Optical Power Conversion via Tunneling of Plasmonic Hot Carriers. *ACS Photonics* **2018**, *5*, 2516–2523.
- (11) Mauser, K. W.; Kim, S.; Mitrovic, S.; Fleischman, D.; Pala, R.; Schwab, K. C.; Atwater, H. A. Resonant Thermoelectric Nanophotonics. *Nat. Nanotechnol.* **2017**, *12*, 770–775.
- (12) Thirugnanasambandam, M.; Iniyar, S.; Goic, R. A Review of Solar Thermal Technologies. *Renewable Sustainable Energy Rev.* **2010**, *14*, 312–322.
- (13) Hartland, G. V. Optical Studies of Dynamics in Noble Metal Nanostructures. *Chem. Rev.* **2011**, *111*, 3858–3887.
- (14) Li, X.; Xiao, D.; Zhang, Z. Landau Damping of Quantum Plasmons in Metal Nanostructures. *New J. Phys.* **2013**, *15*, 023011.
- (15) Khurgin, J. B. How to Deal with the Loss in Plasmonics and Metamaterials. *Nat. Nanotechnol.* **2015**, *10*, 2–6.
- (16) Jiang, L.; Tsai, H.-L. Improved Two-Temperature Model and Its Application in Ultrashort Laser Heating of Metal Films. *J. Heat Transfer* **2005**, *127*, 1167.
- (17) Xie, X.; Cahill, D. G. Thermometry of Plasmonic Nanostructures by Anti-Stokes Electronic Raman Scattering. *Appl. Phys. Lett.* **2016**, *109*, 183104.
- (18) Hugall, J. T.; Baumberg, J. J. Demonstrating Photoluminescence from Au Is Electronic Inelastic Light Scattering of a Plasmonic Metal: The Origin of SERS Backgrounds. *Nano Lett.* **2015**, *15*, 2600–2604.
- (19) Neumann, O.; Urban, A. S.; Day, J.; Lal, S.; Nordlander, P.; Halas, N. J. Solar Vapor Generation Enabled by Nanoparticles. *ACS Nano* **2013**, *7*, 42–49.
- (20) Besteiro, L. V.; Yu, P.; Wang, Z.; Holleitner, A. W.; Hartland, G. V.; Wiederrecht, G. P.; Govorov, A. O. The Fast and the Furious: Ultrafast Hot Electrons in Plasmonic Metastructures. Size and Structure Matter. *Nano Today* **2019**, *27*, 120–145.
- (21) Sun, C.-K.; Vallée, F.; Acioli, L. H.; Ippen, E. P.; Fujimoto, J. G. Femtosecond-Tunable Measurement of Electron Thermalization in Gold. *Phys. Rev. B: Condens. Matter Mater. Phys.* **1994**, *50*, 15337–15348.
- (22) Della Valle, G.; Conforti, M.; Longhi, S.; Cerullo, G.; Brida, D. Real-Time Optical Mapping of the Dynamics of Nonthermal Electrons in Thin Gold Films. *Phys. Rev. B: Condens. Matter Mater. Phys.* **2012**, *86*, 155139.
- (23) Brooks, J. L.; Warkentin, C. L.; Saha, D.; Keller, E. L.; Frontiera, R. R. Toward a Mechanistic Understanding of Plasmon-Mediated Photocatalysis. *Nanophotonics* **2018**, *7*, 1697–1724.
- (24) Yang, J.; Guo, Y.; Lu, W.; Jiang, R.; Wang, J. Emerging Applications of Plasmons in Driving CO<sub>2</sub> Reduction and N<sub>2</sub> Fixation. *Adv. Mater.* **2018**, *30*, 1802227.
- (25) Swearer, D. F.; Zhao, H.; Zhou, L.; Zhang, C.; Robatjazi, H.; Martinez, J. M. P.; Krauter, C. M.; Yazdi, S.; McClain, M. J.; Ringe, E.; et al. Heterometallic Antenna-Reactor Complexes for Photocatalysis. *Proc. Natl. Acad. Sci. U. S. A.* **2016**, *113*, 8916–8920.
- (26) Della Valle, G.; Scotognella, F.; Kandada, A. R. S.; Zavelani-Rossi, M.; Li, H.; Conforti, M.; Longhi, S.; Manna, L.; Lanzani, G.; Tassone, F. Ultrafast Optical Mapping of Nonlinear Plasmon Dynamics in Cu 2-x Se Nanoparticles. *J. Phys. Chem. Lett.* **2013**, *4*, 3337–3344.
- (27) Guo, L.; Xu, X. Ultrafast Spectroscopy of Electron-Phonon Coupling in Gold. *J. Heat Transfer* **2014**, *136*, 1–6.
- (28) Wu, K.; Chen, J.; McBride, J. R.; Lian, T. Efficient Hot-Electron Transfer by a Plasmon-Induced Interfacial Charge-Transfer Transition. *Science* **2015**, *349*, 632–635.
- (29) Wu, S.; Hogan, N.; Sheldon, M. Hot Electron Emission in Plasmonic Thermionic Converters. *ACS Energy Lett.* **2019**, *4*, 2508–2513.
- (30) Greffet, J. J.; Bouchon, P.; Brucoli, G.; Marquier, F. Light Emission by Nonequilibrium Bodies: Local Kirchhoff Law. *Phys. Rev. X* **2018**, *8*, 21008.
- (31) Sergeant, N. P.; Pincon, O.; Agrawal, M.; Peumans, P. Design of Wide-Angle Solar-Selective Absorbers Using Aperiodic Metal-Dielectric Stacks. *Opt. Express* **2009**, *17*, 22800–22812.
- (32) Green, M. A. *Third Generation Photovoltaics: Advanced Solar Energy Conversion*; Kamiya, T., Venghaus, H., Monemar, B., Yamamoto, Y., Eds.; Springer: Berlin, Heidelberg, New York, 2003.
- (33) Ghobadi, A.; Hajian, H.; Gokbayrak, M.; Dereshgi, S. A.; Toprak, A.; Butun, B.; Ozbay, E. Visible Light Nearly Perfect Absorber: An Optimum Unit Cell Arrangement for near Absolute Polarization Insensitivity. *Opt. Express* **2017**, *25*, 27624–27634.
- (34) Chen, F.; Li, Q.; Li, M.; Long, H.; Yao, Y.; Sun, P.; Zhang, J. Simulation of perfect absorber at visible frequencies using TiN-based refractory plasmonic metamaterials. *Opt. Quantum Electron.* **2016**, *48*, 498.
- (35) Shockley, W.; Queisser, H. J. Detailed Balance Limit of Efficiency of P-n Junction Solar Cells. *J. Appl. Phys.* **1961**, *32*, 510–519.
- (36) Li, W.; Fan, S. Nanophotonic Control of Thermal Radiation for Energy Applications. *Opt. Express* **2018**, *26*, 15995–16021.
- (37) Costantini, D.; Lefebvre, A.; Coutrot, A.-L.; Moldovan-Doyen, I.; Hugonin, J.-P.; Boutami, S.; Marquier, F.; Benisty, H.; Greffet, J.-J. Plasmonic Metasurface for Directional and Frequency-Selective Thermal Emission. *Phys. Rev. Appl.* **2015**, *4*, 014023.
- (38) Yu, P.; Besteiro, L. V.; Huang, Y.; Wu, J.; Fu, L.; Tan, H. H.; Jagadish, C.; Wiederrecht, G. P.; Govorov, A. O.; Wang, Z. Broadband Metamaterial Absorbers. *Adv. Opt. Mater.* **2019**, *7*, 1800995.
- (39) Sambles, J. R. An Electron Microscope Study of Evaporating Gold Particles: The Kelvin Equation for Liquid Gold and the Lowering of the Melting Point of Solid Gold Particles. *Proc. R. Soc. London, Ser. A* **1971**, *324*, 339–351.
- (40) Szczepiński, J.; Gyr, L.; Kaeslin, J.; Zenobi, R. Plasmon-Driven Photocatalysis Leads to Products Known from E-Beam and X-Ray-Induced Surface Chemistry. *Nano Lett.* **2018**, *18*, 6740–6749.

- (41) Domke, K. F.; Zhang, D.; Pettinger, B. Enhanced Raman Spectroscopy: Single Molecules or Carbon? *J. Phys. Chem. C* **2007**, *111*, 8611–8616.
- (42) Solomon, E.; Level, A. B. P. *Inorganic Electron Structure and Spectroscopy: Volume 1*; John Wiley & Sons, Inc.: New York, 1999.
- (43) Cai, Y. Y.; Sung, E.; Zhang, R.; Tauzin, L. J.; Liu, J. G.; Ostovar, B.; Zhang, Y.; Chang, W. S.; Nordlander, P.; Link, S. Anti-Stokes Emission from Hot Carriers in Gold Nanorods. *Nano Lett.* **2019**, *19*, 1067–1073.
- (44) Carattino, A.; Calderola, M.; Orrit, M. Gold Nanoparticles as Absolute Nanothermometers. *Nano Lett.* **2018**, *18*, 874–880.
- (45) Huang, J.; Wang, W.; Murphy, C. J.; Cahill, D. G. Resonant Secondary Light Emission from Plasmonic Au Nanostructures at High Electron Temperatures Created by Pulsed-Laser Excitation. *Proc. Natl. Acad. Sci. U. S. A.* **2014**, *111*, 906–911.
- (46) Singh, N. Two-Temperature Model of Non-Equilibrium Electron Relaxation: A Review. *Int. J. Mod. Phys. B* **2010**, *24*, 1141–1158.
- (47) Reguera, J.; Langer, J.; Jiménez De Aberasturi, D.; Liz-Marzán, L. M. Anisotropic Metal Nanoparticles for Surface Enhanced Raman Scattering. *Chem. Soc. Rev.* **2017**, *46*, 3866–3885.
- (48) Foerster, B.; Joplin, A.; Kaefer, K.; Celiksoy, S.; Link, S.; Sönnichsen, C. Chemical Interface Damping Depends on Electrons Reaching the Surface. *ACS Nano* **2017**, *11*, 2886–2893.
- (49) Therrien, A. J.; Kale, M. J.; Yuan, L.; Zhang, C.; Halas, N. J.; Christopher, P. Impact of Chemical Interface Damping on Surface Plasmon Dephasing. *Faraday Discuss.* **2019**, *214*, 59–72.
- (50) Groeneveld, R.; Sprik, R.; Lagendijk, A. Ultrafast Relaxation of Electrons Probed by Surface Plasmons at a Thin Silver Film. *Phys. Rev. Lett.* **1990**, *64*, 784–787.
- (51) Brown, A. M.; Sundararaman, R.; Narang, P.; Goddard, W. A.; Atwater, H. A. Ab Initio Phonon Coupling and Optical Response of Hot Electrons in Plasmonic Metals. *Phys. Rev. B: Condens. Matter Mater. Phys.* **2016**, *94*, 075120.
- (52) Jaque, D.; Martínez Maestro, L.; del Rosal, B.; Haro-Gonzalez, P.; Benayas, A.; Plaza, J. L.; Martín Rodríguez, E.; García Solé, J. Nanoparticles for Photothermal Therapies. *Nanoscale* **2014**, *6*, 9494–9530.
- (53) Ford, R. R.; Pritchard, J. Work Functions of Gold and Silver Films. *Trans. Faraday Soc.* **1971**, *67*, 216–221.
- (54) Hatsopoulos, G. N.; Gyftopoulos, E. P. *Thermionic Energy Conversion, Volume 2: Theory, Technology, and Application*; MIT Press: Cambridge, U.K., 1979.
- (55) Hanke, F.; Björk, J. Structure and Local Reactivity of the Au(111) Surface Reconstruction. *Phys. Rev. B: Condens. Matter Mater. Phys.* **2013**, *87*, 235422.
- (56) Bauer, C.; Abid, J. P.; Girault, H. H. Size Dependence Investigations of Hot Electron Cooling Dynamics in Metal/Adsorbates Nanoparticles. *Chem. Phys.* **2005**, *319*, 409–421.
- (57) Farm, W. S.; Storz, R.; Tom, H. W. K.; Bokor, J. Direct Measurement of Nonequilibrium Electron-Energy Distributions in Sub-Picosecond Laser-Heated Gold Films. *Surf. Sci.* **1993**, *283*, 221–225.
- (58) Hostetler, J. L.; Smith, A. N.; Czajkowski, D. M.; Norris, P. M. Measurement of the Electron-Phonon Coupling Factor Dependence on Film Thickness and Grain Size in Au, Cr, and Al. *Appl. Opt.* **1999**, *38*, 3614.
- (59) Hohlfeld, J.; Wellershoff, S.-S.; Gündde, J.; Conrad, U.; Jähnke, V.; Matthias, E. Electron and Lattice Dynamics Following Optical Excitation of Metals. *Chem. Phys.* **2000**, *251*, 237–258.